 doi:10.20944/preprints202109.0299.v1

Local thermal rates and gradients in laser powder bed fusion metal additive manufacturing method: computer simulation

Hamed Hosseinzadeh [1. 2, *]

[1] *Independent researcher*

[2] *AM Comp Tech Software, Manufacturing Technology Project, NJ, 08012, USA*

[*] *Corresponding author: Hamed Hosseinzadeh, Email: Hamed@uwalumni.com*

Abstract

The powder bed fusion (PBF) metal additive manufacturing (AM) method uses an energy source like a laser to melt the metal powders. The laser can locally melt the metal powders and creates a solid structure as it moves. The complexity of the heat distribution in laser PBF metal AM is one of the main features that need to be accurately addressed and understood to design and manage an optimized printing process. In this research, the dependency of local thermal rates and gradients on print after solidification (in the heat-affected zone) was numerically simulated and studied to provide information for designing the print process. The simulation results were validated by independent experimental results. The simulation shows that the local thermal rates are higher at higher laser power and scan speed. Also, the local thermal gradients increase if the laser power increases. The effect of scan speed on the thermal gradients is opposite during heating versus cooling times. Increasing the scan speed increases the local thermal gradients in the cooling times and decreases the local thermal gradients during the heating. In addition, these simulation results could be used in artificial intelligence (AI) and machine learning for developing digital additive manufacturing.

Keywords: Metal 3D printing, Additive manufacturing, Powder bed fusion, Thermal simulation, Thermal history

 doi:10.20944/preprints202109.0299.v1

1. Introduction

The metal additive manufacturing (AM) process is using a heat source to deposit the melted materials layer by layer. Metal Am or metal 3D printing is rapid prototyping, and it can be beneficial for producing non-structural (design purposes) and structural applications [1]. ASTM has categorized additive manufacturing processes as Directed Energy Deposition (DED) and Powder Bed Fusion (PBF). Recently, metal 3D printing became more popular, and the microstructure/mechanical properties of the printed sample were experimentally studied [2–7]. This subject shows the importance of understanding the thermal history during metal 3D printing as the microstructure is controlling by the local thermal history. Although there are some examples of 3D printed samples ready for application without additional postprocessing [8,9], the mechanical properties and microstructure of the metal 3d printed samples are not fully reliable for applications without postprocessing, especially for load-bearing applications. So, most printed samples need additional postprocessing [10,11], and the effect of heat treatment on mechanical properties/microstructure needs to be studied in detail [12]. Thermal history during printing and melting/solidification conditions are controlling subsequent microstructure (thermal rates), thermal deformation (thermal gradients), and thermal stress[13]. The simulation can produce details about thermal history during printing [7,14–17], and the computational results could be used for estimating the local microstructure, thermal deformations, and the optimization of the metal AM process. Several researchers coupled macroscale thermal simulation coupled with mesoscale microstructural evaluation [18–21]. There are several published kinds of research on mesoscale microstructural simulations for powder bed-based additive manufacturing in the first layer of the print [22–27]. In addition, there are researches on addressing the grain structure of the additively manufactured materials, especially for powder bed fusion [27–30]. There are some experimental and computational investigations and papers that discussed thermal stress and deformation in additively manufactured metallic alloys [1,31–33]. Thermal stress and deformation of additively manufactured are about several hundred MPa [34,35] and several micrometers for small samples [36–39], respectively. This level of deformation is high enough, especially for complex shapes to reject the printed sample for application. So, we need to investigate some methods to optimize microstructure, defects, and reduce the level of thermal stress and deformation. The main step is the thermal simulation, the estimation of the local heating/cooling rates and gradients, and their dependency on print parameters.

Experiments have some limitations for measuring the local thermal history during metal AM that simulation can cover. It is not easy to use thermocouples directly measuring the heating/cooling curves and subsequent thermal rates and gradients due to the nature of the sample fabrication in the LPBF method. In addition, using the thermal camera is also imposed another kind of limitation. The thermal camera is accurate at high temperatures and mostly useful for measuring the melt-pool temperature before tarting the solidifications [40]. In addition, thermal cameras measure surface temperature. The simulation can be an efficient method for estimating the thermal rates and gradients and also covering the experimental limitations in measuring the local thermal history during printing metallic samples with the LPBF method.

In this research, the thermal history is numerically simulated, and the dependency of local thermal rates and gradients on print parameters was estimated to provide information for understanding and designing the print process.

Preprints (www.preprints.org) | NOT PEER-REVIEWED | Posted: 17 September 2021 doi:10.20944/preprints202109.0299.v1

2. Simulation method

AM Comp Tech software academic version was used for thermal simulation of laser PBF metal AM in this research. The software solves conservative equations (conservation of energy) by finite difference numerical method. Equation 1 was used for thermal analysis in which ρ is density, C_p is the specific heat, T is temperature, t is time, λ_i is the thermal conductivity, and S is the source of heat. h represents both the thermal convection and radiation coefficients. The value of β was considered to be 0.9, as recommended for steels [41].

$$\rho C_p \frac{\partial T}{\partial t} = \nabla.(\lambda_i \nabla T) + S \qquad (1)$$

$$-\nabla.(\lambda_i \nabla T) = h(T - T_\infty) \qquad (2)$$

$$h = 0.00241 \times \beta \times T^{1.61}$$

The energy balance in equation (2) was applied as a thermal boundary condition on the top surface of the simulation domain, which is not under the laser. This equation has both the physical meaning of thermal convection and radiation.

The used density was 7500 kg.m^3, the temperature-dependent thermal conductivity was 10^{-4}×T×6.747 W.m^{-1}.K^{-1}, (T is temperature), and the specific heat capacity was 500 J.kg^{-1}K^{-1}.

The laser heat input with a Gaussian profile, defined with equation 2, was applied to the top surface of the powder [42] as the energy source.

$$\text{Laser heat input} = \frac{fq\eta}{r^2} \; e^{\left(-\frac{f(x^2+y^2)}{r^2}\right)} \qquad (2)$$

where *f* is the heat distribution factor, *q* is the Laser power, *η* is the absorption coefficient, *x* and *y* are the distances from the node at the center of the laser, and *r* is the radius of the laser spot. In this simulation, f is 1.7 and η is 0.2. Also, a telescopic method was used for applying volumetric heating since the laser can penetrate the metal powders [43].

The boundary condition on the top side of the simulation domain is the air and heat input of the laser (laser spot). The rest of the boundary condition is at the interface of the printed sample (bulk metal) and the metal powders. The thermal properties of the metal powders are assumed like bulk metal with porosity. So, the thermal properties of metal powders are calculated by multiplying metal powder density to bulk metal's thermal properties [44]. 0.8 percent is the density of the metal powders in this simulation.

The used major assumptions for simplicity are not considering the latent heat of fusion and metal evaporation. These two assumptions will introduce some errors in the simulation results and an overestimation will be predicted in melt-pool temperature and the subsequent thermal rates/gradients. Anyway, it is also expected that the trend of the thermal rates and gradients at different print parameters could be correctly estimated by this numerical model.

Preprints (www.preprints.org) | NOT PEER-REVIEWED | Posted: 17 September 2021 doi:10.20944/preprints202109.0299.v1

3. Results and discussions

The thermal history in laser powder bed fusion (LPBF) is complicated due to the fast movement of the laser and complex print pattern. Improving our understanding of the local thermal (heating and cooling) rates and gradients is essential in optimizing the LPBF metal additive manufacturing process. Thermal rates and gradients were simulated by 3D numerical simulation with AM Comp Tech software – academic version. Sixteen simulations were performed to study the effect of scan speed and laser power on the thermal history. The selected print parameters have been shown in table 1. The layer thickness, hatch-spacing, and print pattern were kept constant. The print pattern and scanning strategy is a zig-zag pattern with a rotation angle of 90°.

Table 1 *The selected print parameters in each simulation.*

#	Laser Power (W)	Scan Speed (mm/s)	Hatch-spacing (µm)	Layer Thickness (µm)
CASE 1	*100*	*500*	*80*	*30*
CASE 2	*100*	*800*	*80*	*30*
CASE 3	*100*	*1300*	*80*	*30*
CASE 4	*100*	*1600*	*80*	*30*
CASE 5	*150*	*500*	*80*	*30*
CASE 6	*150*	*800*	*80*	*30*
CASE 7	*150*	*1300*	*80*	*30*
CASE 8	*150*	*1600*	*80*	*30*
CASE 9	*200*	*500*	*80*	*30*
CASE 10	*200*	*800*	*80*	*30*
CASE 11	*200*	*1300*	*80*	*30*
CASE 12	*200*	*1600*	*80*	*30*
CASE 13	*250*	*500*	*80*	*30*
CASE 14	*250*	*800*	*80*	*30*
CASE 15	*250*	*1300*	*80*	*30*
CASE 16	*250*	*1600*	*80*	*30*

The selected simulation domain is the smallest possible meaningful size which is shown in *figure 1a*. In this simulation, the simulation domain is a cube with two hatch-spacing by one hatch-spacing by three powder layers volume. The example of 3D thermal simulation results is shown in *figure 1b*. The four points are selected at a cross-section shown in *figure 2* to export thermal history, rates, and gradients.

Preprints (www.preprints.org) | NOT PEER-REVIEWED | Posted: 17 September 2021 doi:10.20944/preprints202109.0299.v1

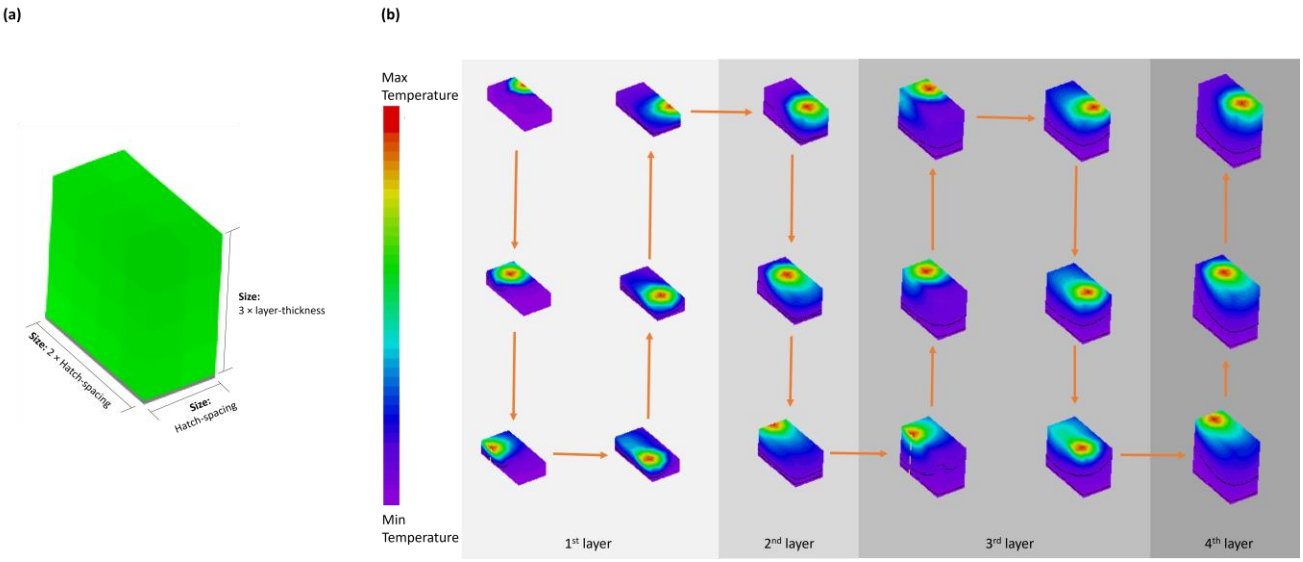

Fig 1 *(a) the simulation domain and (b) the spatial presentation of the temperature distribution during printing of four layers on each other (LPBF metal AM).*

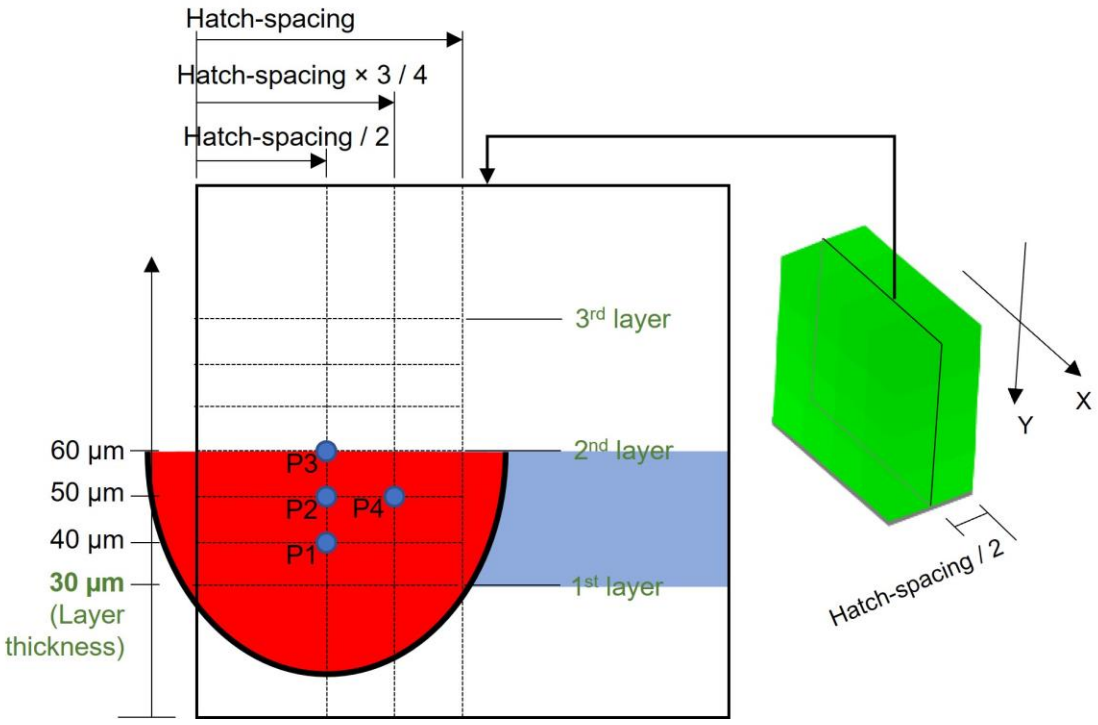

Fig 2 *A selected plane at the middle of the simulation domain and four points (P1, P2, P3, and P4) were appointed at different positions in the melt-pool to extract the cooling rates and gradients.*

Preprints (www.preprints.org) | NOT PEER-REVIEWED | Posted: 17 September 2021 doi:10.20944/preprints202109.0299.v1

The simulated and exported heating/cooling curve of CASE 1 at P1 is shown in *figure 3a*. The heating/cooling curves of the solidified region and heat-affected zone (HAZ) were used for calculating thermal rates (*figure 3b*). The six thermal peaks shown in *figure 3a* are related to the heat source movement. This subject and the position of P1 relative to the melt pool are illustrated in *figure 3c* for each peak. The first three peaks (1 to 3) are related to the melting of the powders or the remelting of the solidified melt pool. That is to say, P1 is inside the melt-pool at peaks 1 to 3. The position of P1 for the three last thermal peaks (4 to 6) are related to the heat-affected zone (HAZ) in the solid-state. The maximum temperature of peaks 4 to 6 is lower than the melting point.

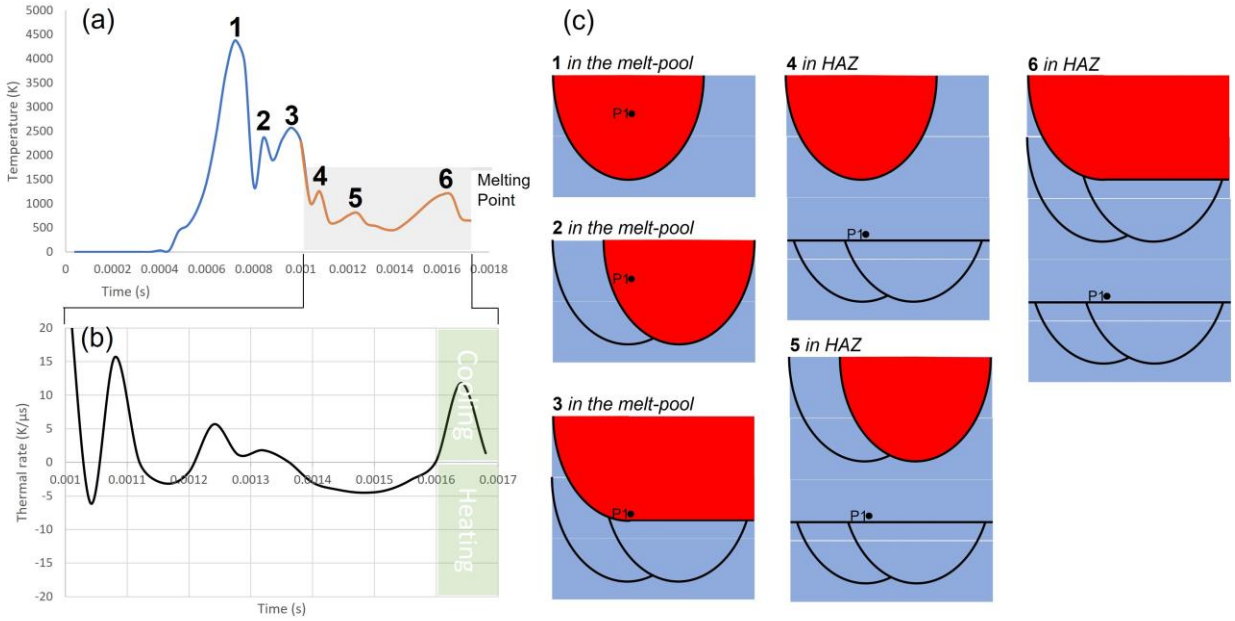

Fig 3 *(a) A simulated cooling curve in LPBF method, (b) subsequent thermal rate at P1 in HAZ, and (c) a schematic of how laser melts the metal powders (melt-pool: red region) and creates the sample layer by layer.*

The simulation results show that the thermal rate values of CASE 1 are between 5 to 20 K/µs at P1 after solidification in the HAZ (*figure 3b*). The thermal rate has a higher value close to the melting point and has lower values in HAZ. In addition, the cooling rates have higher values than the values of heating rates in HAZ (*figure 3b*).

In the following topics, the effect of scan speed and laser power was discussed on the local thermal rates and gradients at P1, P2, P3, and P4.

3.1. Thermal rates

Thermal rate or heating/cooling rate is controlling the final microstructure. Understanding the effect of scan speed and laser power on the thermal rates can help to have a better design on the print process and controlling the final microstructure. Also, the validated simulation results combined with artificial intelligence (AI) can be used later for simultaneously controlling the laser PBF metal AM process.

Experimental results of the local thermal rates are mostly limited to the surface of the melt-pool and during cooling of the molten metal from the evaporation temperature to melting temperature. So, we

Preprints (www.preprints.org) | NOT PEER-REVIEWED | Posted: 17 September 2021 doi:10.20944/preprints202109.0299.v1

are limited to such kinds of experimental results for the validation of the numerical model and simulation. Experiments show that the peak cooling rate occurs immediately after the laser is switched off and is approximately 40 K/µs at the surface of the melt-pool. In addition, the cooling rates have any value between 1 to 40 K/µs at the surface of the melt-pool during cooling from the evaporation temperature [40]. In this research, P3 is at the surface of the melt-pool in the simulation domain. The simulated results of the cooling curve and thermal rates at P3 between evaporation temperature (~4000 K) to 3000 K are shown in *figure 4*. The simulation result shows that the cooling rate has a value around 46 K/µs at 4000 K and drops to 7 K/µs at 3000 K after switching off the laser. So, the simulation result shows consistency with the experimental results. Besides, checking the exact values of the simulation results with experimental results to validate the simulation, the variation and general trend of the thermal rates measured by experiments can be used to check the validation of simulation results. The experimental results discussed the higher cooling rates at higher heat input [45,46] and scan speed [47]). The simulation results of this research can predict the trend of the dependency of the cooling rate on the scan speed and laser power the same as the experimental measurements. So, it can be concluded that the thermal simulation of this research can be used to study the effect of print parameters on the local thermal rates. This subject will discuss further in following topics. The thermal rates at P1, P2, and P3 have been compared and the effect of scan speed and laser power on the thermal rates at these points have been discussed in HAZ.

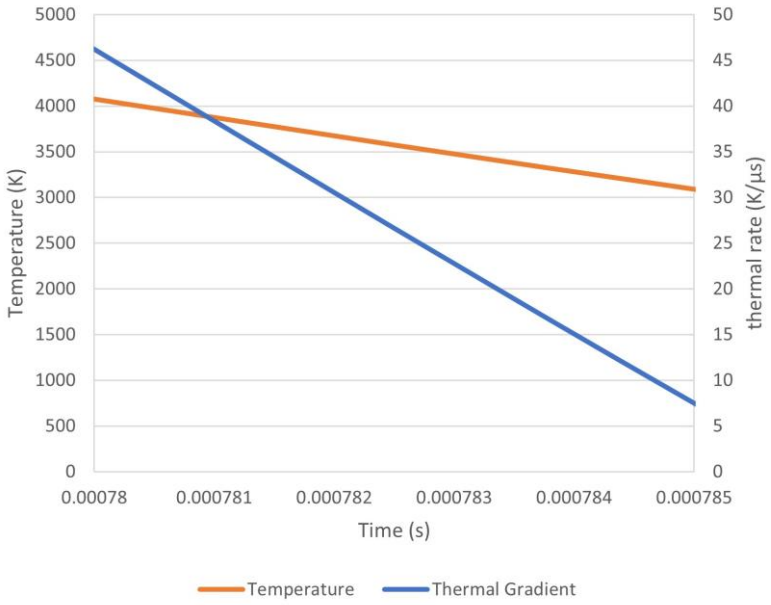

Fig 4 *The simulated thermal rate in the melt-pool during cooling from 4000 K to 3000 K temperature range after the laser is switched off.*

P3 is at the surface of the melt pool. P2 and P1 are in the melt-pool (*figure 2*). Simulation shows the lower thermal rate value at P1 than the values at P2 and P3 after solidification. This subject is shown in *figure 5*. The positive value of the thermal rate means cooling region and the negative value means heating region.

Preprints (www.preprints.org) | NOT PEER-REVIEWED | Posted: 17 September 2021 doi:10.20944/preprints202109.0299.v1

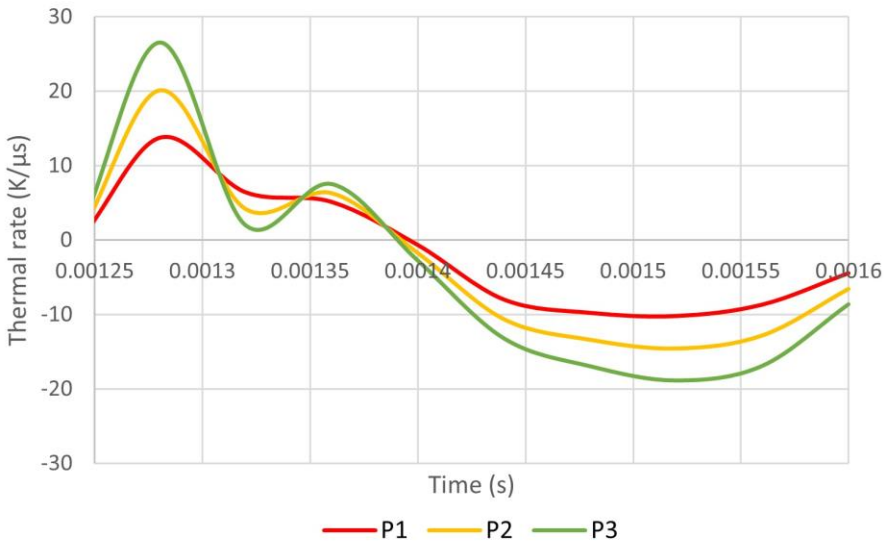

Fig 5 *The thermal rates at P1, P2, and P3 (Laser power: 250 W and scan speed: 500 mm/s).*

The effect of scan speed on the thermal rates at P1, P2, and P3 are summarized in *figure 6*. The results show higher thermal rates at higher scan speeds.

Fig 6 *The effect of scan speed on the thermal rates at P1, P2, and P3 (Laser power: 100 W).*

Also, the maximum thermal rates (Positive peaks: cooling and negative peaks: heating) are highest at the surface of the melt-pool (P3) and will be lower at the points (like P2) in the melt-pool. In addition, the maximum thermal rates have lower values at the deeper points compare to P2 (like P1).

The effect of laser power on the thermal rates at P1, P2, and P3 are summarized in *figure 7*. The results show higher thermal rates at higher laser power. Also, the values of the thermal rates increase from *figure 7a* to *7d* which means the local thermal rates will be higher by increasing both laser power and scan speed. This subject is also shown in *figure 8* (The dependency of the maximum cooling rate at P1 with different scan speeds and laser powers). As conclusion and example, simulation results (if the scan speed changes in 500 to 1300 mm/s range) show a 0.5×10^{-2} K/µs increase in the cooling rate (at P1) by every 1 mm/s increase in the scan speed if the laser power and hatch spacing are 200 W and 80 µm, respectively. Also, the simulation results (if the laser power changes in 100 to 250 W range) show a 0.1 K/µs increase in the cooling rate (at P1) by every 1 W increase in the laser power if the scan speed and hatch spacing are 1000 mm/s and 80 µm, respectively.

Preprints (www.preprints.org) | NOT PEER-REVIEWED | Posted: 17 September 2021 doi:10.20944/preprints202109.0299.v1

The same scenario of thermal cooling rates like P1 is at P2 and P3 but with higher values. As a general summary, the local thermal rates at any point in HAZ will be increased by the increase of laser power and scan speed.

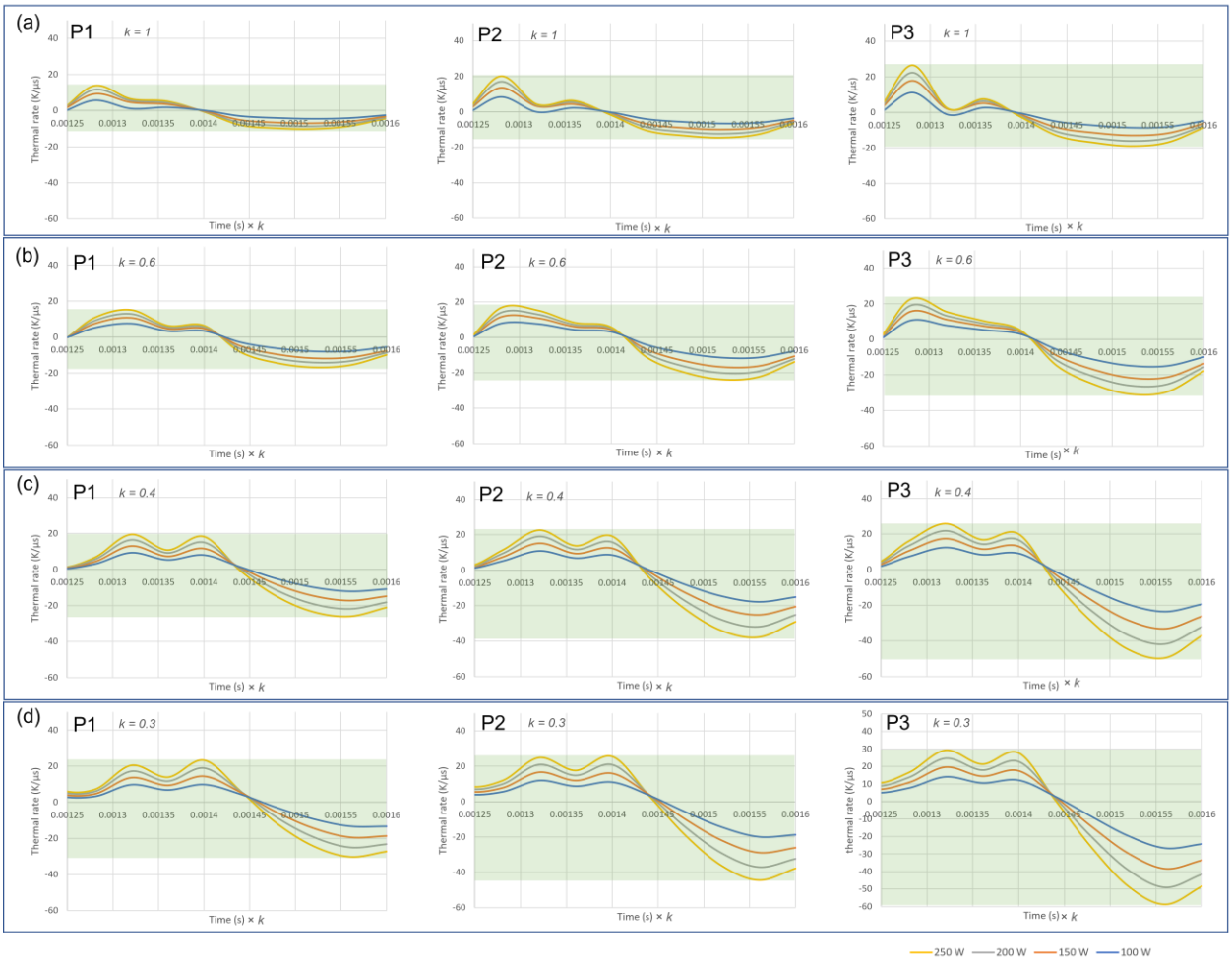

Fig 7 *The simultaneous effect of laser powers (100 to 250 W) and scan speeds on the thermal rates at P1. (a) 500 mm/s, (b) 800 mm/s, (c) 1300 mm/s, and (d) 1600 mm/s.*

Preprints (www.preprints.org) | NOT PEER-REVIEWED | Posted: 17 September 2021 doi:10.20944/preprints202109.0299.v1

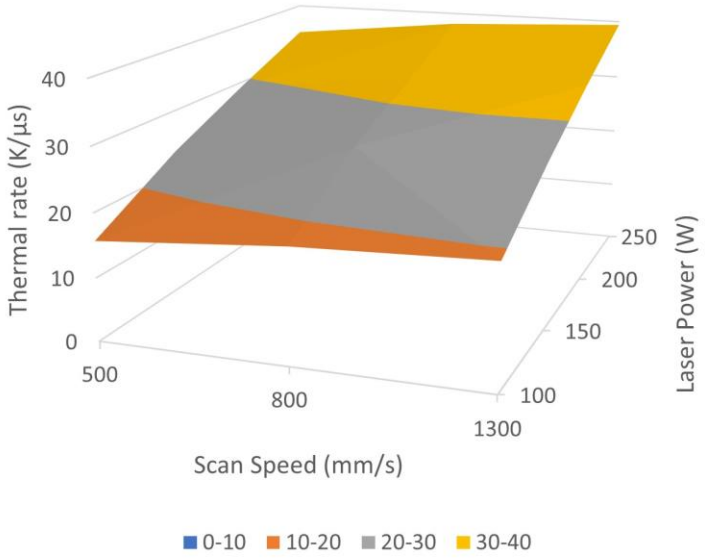

Fig 8 *The maximum cooling rate of P1 in HAZ at different scan speeds and laser powers.*

3.2. Thermal gradients

Thermal gradients of the LPBF method are in the 5–20 K/µm range in the melt-pool and this temperature gradient drops to approximately 5 K/µm as the melting temperature is approached (Laser power: 170 W, hatch spacing: 65 um, and scan speed: 1250 mm/s) [40]. The simulation result with an almost similar print parameters set shows that the absolute value of thermal gradients at the melting point is about 5 K/µm and lower which is close to the experimental results (*figure 9*). In the next topics, the effect of scan speeds and laser powers on the local thermal gradients are discussed with this validated numerical simulation.

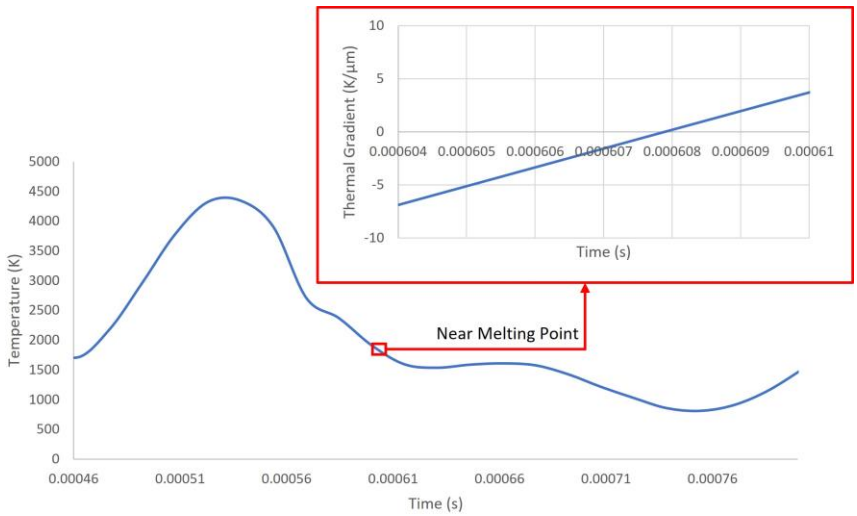

Fig 9 *The heating and cooling rate at point P1 and the thermal gradient close to the melting point (Laser power: 150 W, hatch spacing: 80 um, and scan speed: 1300 mm/s).*

Preprints (www.preprints.org) | NOT PEER-REVIEWED | Posted: 17 September 2021 doi:10.20944/preprints202109.0299.v1

3.2.1. The thermal gradient at P2 (X-direction):

The effect of laser power on the thermal gradients at P2 in the X direction has been shown in *figure 10*. After solidification and in HAZ, the thermal gradients change between negative and positive values in the -80 K/µm to 100 K/µm range. The thermal gradient is higher at higher laser power.

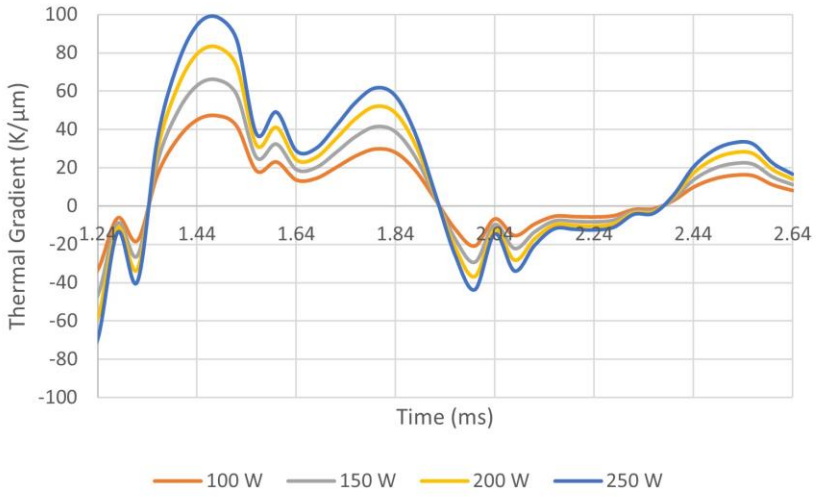

Fig 10 *The effect of laser powers on the thermal gradients at P2 in the X direction (Scan speed: 500 mm/s).*

The effect of scan speeds on the thermal gradients at P2 in the X direction has been shown in *figure 11*. After solidification and in HAZ, the thermal gradients change between negative and positive values in the -30 K/µm to 90 K/µm range. The thermal gradient is lower at higher scan speed during heating times (the yellow region in *figure 11*). Also, the thermal gradient is higher at higher scan speed during cooling times (the green region in *figure 11*).

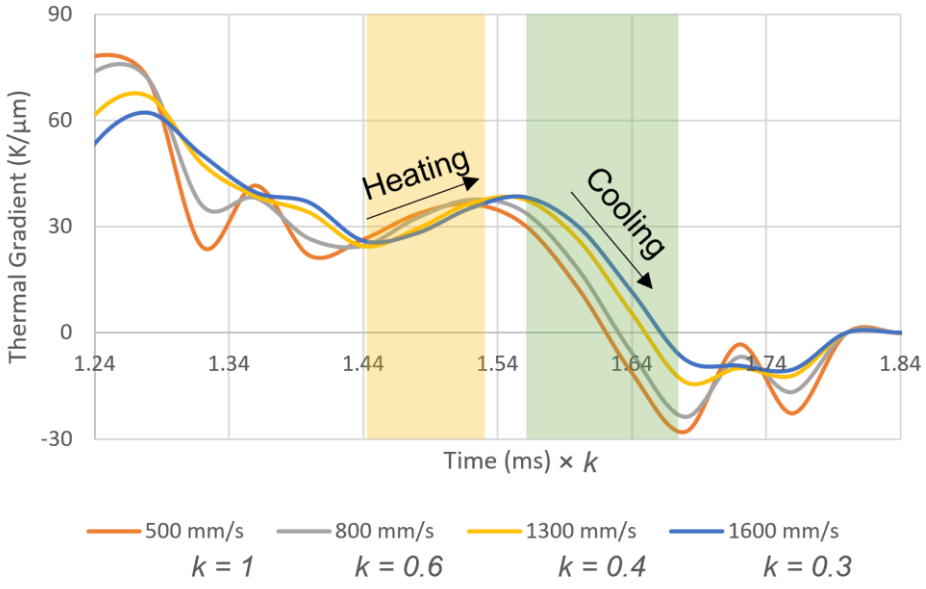

Fig 11 *The effect of scan speeds on the thermal gradients at P2 in the X direction (Laser power: 150 W).*

Preprints (www.preprints.org) | NOT PEER-REVIEWED | Posted: 17 September 2021 doi:10.20944/preprints202109.0299.v1

3.2.2. The thermal gradient at P2 (Y-direction):

The effect of laser power on the thermal gradients at P2 in the Y direction has been shown in *figure 12*. After solidification and in HAZ, the thermal gradients have positive values between 1 K/µm to 160 K/µm. The thermal gradient is higher at higher laser power.

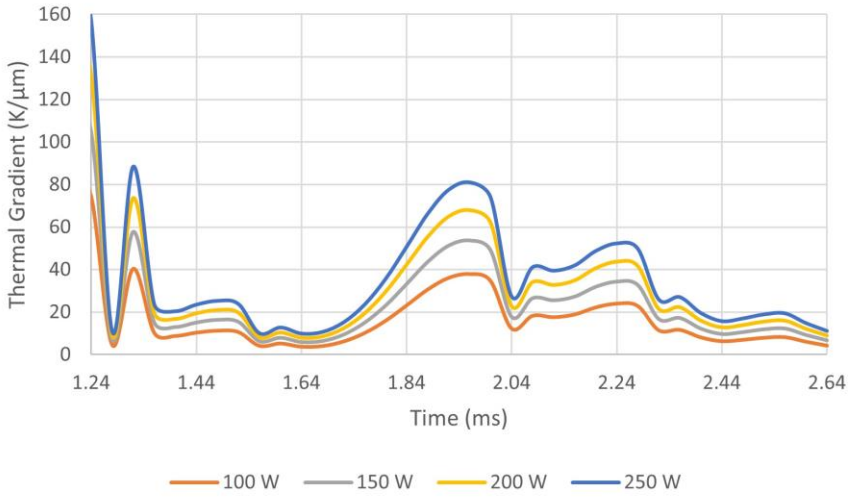

Fig 12 *The effect of laser powers on the thermal gradients at P2 in the Y direction (Scan speed: 500 mm/s).*

The effect of scan speeds on the thermal gradients at P2 in the Y direction has been shown in *figure 13*. After solidification and in HAZ, the thermal gradients have positive values lower than 60 K/µm. The thermal gradient is lower at higher scan speed during heating times (the yellow region in *figure 13*). Also, the thermal gradient is higher at higher scan speed during cooling times (the green region in *figure 13*).

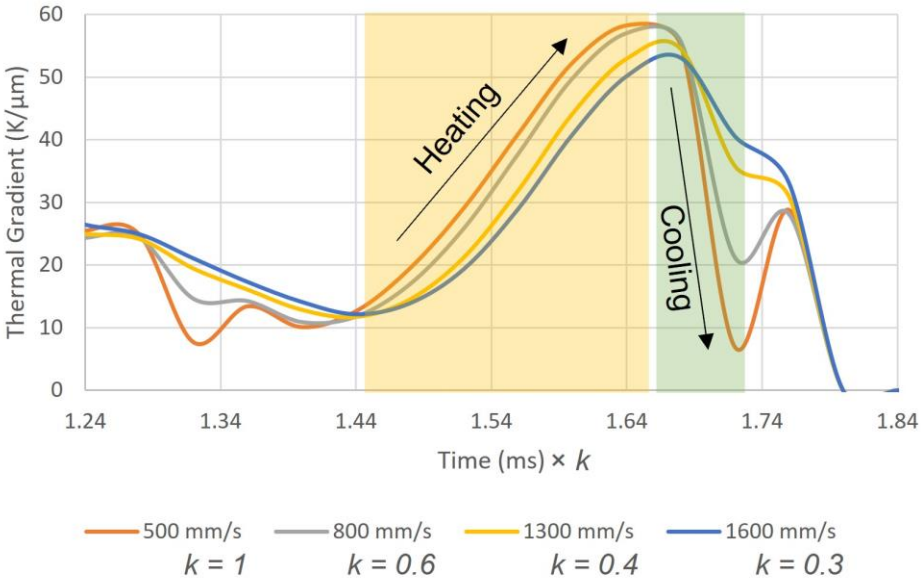

Fig 13 *The effect of scan speeds on the thermal gradients at P2 in the Y direction (Laser power: 150 W).*

 doi:10.20944/preprints202109.0299.v1

4. Conclusions

The local thermal rates and gradients control the local microstructure and the local thermal stress/strain. In this research, the dependency of the local thermal rates and gradients on the scan speeds and laser powers are studied by validated numerical simulations. The highlighted results are:

1. The local thermal rates have higher values at higher laser powers and scan speeds. The simulated cooling rates have values between 1 to 30 K/µs in HAZ.
2. The simulation results (if the scan speed changes in 500 to 1300 mm/s range) show a 0.5×10^{-2} K/µs increase in the cooling rate (at P1) by every 1 mm/s increase in the scan speed if the laser power and hatch spacing are 200 W and 80 µm, respectively.
3. The simulation results (if the laser power changes in the 100 to 250 W range) show a 0.1 K/µs increase in the cooling rate (at P1) by every 1 W increase in the laser power if the scan speed and hatch spacing are 1000 mm/s and 80 µm, respectively.
4. The thermal gradient is lower at a higher scan speed during heating times. Also, the thermal gradient is higher at a higher scan speed during cooling times. The absolute values of the simulated cooling rates are mostly lower than 100 K/µm in HAZ.

References

[1] Debroy T, Wei HL, Zuback JS, Mukherjee T, Elmer JW, Milewski JO, et al. Progress in Materials Science Additive manufacturing of metallic components – Process , structure and properties 2018;92:112–224.

[2] Sergio M, Lima F De, Sankaré S. Microstructure and mechanical behavior of laser additive manufactured AISI 316 stainless steel stringers Microstructure and mechanical behavior of laser additive manufactured AISI 316 stainless steel stringers. J Mater 2014;55:526–32. https://doi.org/10.1016/j.matdes.2013.10.016.

[3] Shi X, Ma S, Liu C, Wu Q, Lu J, Liu Y, et al. Materials Science & Engineering A Selective laser melting-wire arc additive manufacturing hybrid fabrication of Ti-6Al-4V alloy : Microstructure and mechanical properties. Mater Sci Eng A 2017;684:196–204. https://doi.org/10.1016/j.msea.2016.12.065.

[4] Pham MS, Dovgyy B, Hooper PA. Materials Science & Engineering A Twinning induced plasticity in austenitic stainless steel 316L made by additive manufacturing. Mater Sci Eng A 2017;704:102–11. https://doi.org/10.1016/j.msea.2017.07.082.

[5] Croteau JR, Grif S, Rossell MD, Leinenbach C, Kenel C, Jansen V, et al. Acta Materialia Microstructure and mechanical properties of Al-Mg-Zr alloys processed by selective laser melting 2018;153:35–44. https://doi.org/10.1016/j.actamat.2018.04.053.

[6] Nassar AR, Reutzel EW. Additive Manufacturing of Ti-6Al-4V Using a Pulsed Laser Beam. Metall Mater Trans A 2015;46A:2781–9. https://doi.org/10.1007/s11661-015-2838-z.

[7] Shamsaei N, Yadollahi A, Bian L, Thompson SM. An overview of Direct Laser Deposition for additive manufacturing; Part II: Mechanical behavior, process parameter optimization and control. Addit Manuf 2015;8:12–35. https://doi.org/10.1016/j.addma.2015.07.002.

[8] Shayesteh Moghaddam N, Saedi S, Amerinatanzi A, Hinojos A, Ramazani A, Kundin J, et al. Achieving superelasticity in additively manufactured NiTi in compression without post-process heat treatment. Sci Rep 2019;9:1–11. https://doi.org/10.1038/s41598-018-36641-4.

[9] Wang YM, Voisin T, McKeown JT, Ye J, Calta NP, Li Z, et al. Additively manufactured hierarchical stainless steels with high strength and ductility. Nat Mater 2018;17:63–70. https://doi.org/10.1038/NMAT5021.

[10] Li J, Cheng X, Li Z, Zong X, Zhang S, Wang H. Materials Science & Engineering A Improving the mechanical properties of Al-5Si-1Cu-Mg aluminum alloy produced by laser additive manufacturing with post-process heat treatments. Mater Sci Eng A 2018;735:408–17. https://doi.org/10.1016/j.msea.2018.08.074.

[11] Zhuo L, Wang Z, Zhang H, Yin E, Wang Y, Xu T, et al. Effect of post-process heat treatment on microstructure and properties of selective laser melted AlSi10Mg alloy. Mater Lett 2019;234:196–200. https://doi.org/10.1016/j.matlet.2018.09.109.

[12] Yadollahi A, Shamsaei N, Thompson SM, Seely DW. Effects of process time interval and heat treatment on the mechanical and microstructural properties of direct laser deposited 316L stainless steel. Mater Sci Eng A 2015;644:171–83. https://doi.org/10.1016/j.msea.2015.07.056.

[13] Cunningham CR, Flynn JM, Shokrani A, Dhokia V, Newman ST. Invited review article : Strategies and processes for high quality wire arc additive manufacturing. Addit Manuf 2018;22:672–86. https://doi.org/10.1016/j.addma.2018.06.020.

[14] Steuben JC, Birnbaum AJ, Michopoulos JG, Iliopoulos AP. Enriched analytical solutions for additive manufacturing modeling and simulation. Addit Manuf 2019;25:437–47. https://doi.org/10.1016/j.addma.2018.10.017.

[15] Peng H, Ghasri-khouzani M, Gong S, Attardo R, Ostiguy P, Aboud B, et al. Fast prediction of thermal distortion in metal powder bed fusion additive manufacturing : Part 1 , a thermal circuit network model. Addit Manuf 2018;22:852–68. https://doi.org/10.1016/j.addma.2018.05.023.

[16] Mcmillan M, Leary M, Brandt M. Computationally efficient finite difference method for metal additive manufacturing : A reduced-order DFAM tool applied to SLM. Mater Des 2017;132:226–43. https://doi.org/10.1016/j.matdes.2017.06.058.

[17] Cheng L, Yang Q, Zhang P, Cheng L, Min Z, Chyu M, et al. Finite element modeling and validation of thermomechanical behavior of Ti- 6Al-4V in directed energy deposition additive manufacturing Finite element modeling and validation of thermomechanical behavior of Ti-6Al-4V in directed energy deposition additive . Addit Manuf 2016;12:169–77. https://doi.org/10.1016/j.addma.2016.06.012.

[18] Panwisawas C, Sovani Y, Anderson MJ, Turner R, Palumbo NM, Saunders BC, et al. A Multi-Scale Multi-Physics Approach to Modelling of Additive Manufacturing in Nickel-Based Superalloys. Superalloys2016 Warrendale, TMS 2016:1021–30. https://doi.org/10.1002/9781119075646.ch108.

[19] Methods C, Mech A, Yan W, Lian Y, Yu C, Kafka OL, et al. An integrated process – structure – property modeling framework for additive manufacturing. Comput Methods Appl Mech Engrg 2018;339:184–204. https://doi.org/10.1016/j.cma.2018.05.004.

[20] Zhang Z, Tan ZJ, Yao XX, Hu CP, Ge P, Wan ZY, et al. Numerical methods for microstructural evolutions in laser additive manufacturing 2018. https://doi.org/10.1016/j.camwa.2018.07.011.

[21] Michopoulos JG, Iliopoulos AP, Steuben JC, Birnbaum AJ, Lambrakos SG. On the multiphysics modeling challenges for metal additive manufacturing processes. Addit Manuf 2018;22:784–99. https://doi.org/10.1016/j.addma.2018.06.019.

[22] Zinovieva O, Zinoviev A, Ploshikhin V. Three-dimensional modeling of the microstructure evolution during metal additive manufacturing. Comput Mater Sci 2018;141:207–20. https://doi.org/10.1016/j.commatsci.2017.09.018.

[23] Rai A, Helmer H, Körner C. Simulation of grain structure evolution during powder bed based additive manufacturing. Addit Manuf 2017;13:124–34. https://doi.org/10.1016/j.addma.2016.10.007.

[24] Rodgers TM, Madison JD, Tikare V. Simulation of metal additive manufacturing microstructures using kinetic Monte Carlo. Comput Mater Sci 2017;135:78–89. https://doi.org/10.1016/j.commatsci.2017.03.053.

[25] Lu L, Sridhar N, Zhang Y. Acta Materialia Phase field simulation of powder bed-based additive manufacturing. Acta Mater 2018;144:801–9. https://doi.org/10.1016/j.actamat.2017.11.033.

[26] Sahoo S, Chou K. Phase-field simulation of microstructure evolution of Ti-6Al-4V in electron beam additive manufacturing process. Addit Manuf 2016;9:14–24. https://doi.org/10.1016/j.addma.2015.12.005.

[27] Liu PW, Ji YZ, Wang Z, Qiu CL, Antonysamy AA, Chen LQ, et al. Investigation on evolution mechanisms of site-specific grain structures during metal additive manufacturing. J Mater Process Technol 2018;257:191–202. https://doi.org/10.1016/j.jmatprotec.2018.02.042.

[28] Yan F, Xiong W, Faierson EJ. Grain Structure Control of Additively Manufactured 2017:1–11. https://doi.org/10.3390/ma10111260.

[29] Markl M, Körner C. Multiscale Modeling of Powder Bed–Based Additive Manufacturing. Annu Rev Mater Res 2016;46:93–123. https://doi.org/10.1146/annurev-matsci-070115-032158.

[30] Koepf JA, Gotterbarm MR, Markl M, Körner C. 3D multi-layer grain structure simulation of powder bed fusion additive manufacturing. Acta Mater 2018;152:119–26. https://doi.org/10.1016/j.actamat.2018.04.030.

[31] Wu AS, Brown DW, Kumar M, Gallegos GF, King WE. An Experimental Investigation into Additive Manufacturing-Induced Residual Stresses in 316L Stainless Steel. Metall Mater Trans A Phys Metall Mater Sci 2014;45:6260–70. https://doi.org/10.1007/s11661-014-2549-x.

[32] Zaeh MF, Branner G. Investigations on residual stresses and deformations in selective laser melting. Prod Eng 2010;4:35–45. https://doi.org/10.1007/s11740-009-0192-y.

[33] Moat RJ, Pinkerton AJ, Li L, Withers PJ, Preuss M. Residual stresses in laser direct metal deposited Waspaloy. Mater Sci Eng A 2011;528:2288–98. https://doi.org/10.1016/j.msea.2010.12.010.

[34] Johnson KL, Rodgers TM, Underwood OD, Madison JD, Ford KR, Whetten SR, et al. Simulation and experimental comparison of the thermo-mechanical history and 3D microstructure evolution of 304L stainless steel tubes manufactured using LENS. Comput Mech 2018;61:559–74. https://doi.org/10.1007/s00466-017-1516-y.

[35] Peng H, Ghasri-Khouzani M, Gong S, Attardo R, Ostiguy P, Rogge RB, et al. Fast prediction of thermal distortion in metal powder bed fusion additive manufacturing: Part 2, a quasi-static thermo-mechanical model. Addit Manuf 2018;22:869–82. https://doi.org/10.1016/j.addma.2018.05.001.

[36] Santos LS, Gupta SK, Bruck HA. Simulation of buckling of internal features during selective laser sintering of metals. Addit Manuf 2018;23:235–45. https://doi.org/10.1016/j.addma.2018.08.002.

[37] Mayer T, Brändle G, Schönenberger A, Eberlein R. Simulation and validation of residual deformations in additive manufacturing of metal parts. Heliyon 2020;6. https://doi.org/10.1016/j.heliyon.2020.e03987.

[38] Megahed M, Mindt HW, N'Dri N, Duan H, Desmaison O. Metal additive-manufacturing process and residual stress modeling. vol. 5. Integrating Materials and Manufacturing Innovation; 2016. https://doi.org/10.1186/s40192-016-0047-2.

[39] Stender ME, Beghini LL, Sugar JD, Veilleux MG, Subia SR, Smith TR, et al. A thermal-mechanical finite element workflow for directed energy deposition additive manufacturing process modeling. Addit Manuf 2018;21:556–66. https://doi.org/10.1016/j.addma.2018.04.012.

[40] Hooper PA. Melt pool temperature and cooling rates in laser powder bed fusion. Addit Manuf 2018;22:548–59. https://doi.org/10.1016/j.addma.2018.05.032.

[41] Haddad-Sabzevar M, Haerian A, Seied-Hossein-Zadeh H. A stochastic model for austenite phase formation during arc welding of a low alloy steel. J Mater Process Technol 2009. https://doi.org/10.1016/j.jmatprotec.2008.08.039.

[42] He X, Elmer JW, Debroy T. Heat transfer and fluid flow in laser microwelding. J Appl Phys 2005;97. https://doi.org/10.1063/1.1873032.

[43] Bayat M, Mohanty S, Hattel JH. A systematic investigation of the effects of process parameters on heat and fluid flow and metallurgical conditions during laser-based powder bed fusion of Ti6Al4V alloy. Int J Heat Mass Transf 2019;139:213–30. https://doi.org/10.1016/j.ijheatmasstransfer.2019.05.017.

[44] Foroozmehr A, Badrossamay M, Foroozmehr E, Golabi S. Finite Element Simulation of Selective Laser Melting process considering Optical Penetration Depth of laser in powder bed. Mater Des 2016;89:255–63. https://doi.org/10.1016/j.matdes.2015.10.002.

[45] Lane B, Heigel J, Ricker R, Zhirnov I, Khromschenko V, Weaver J, et al. Measurements of Melt Pool Geometry and Cooling Rates of Individual Laser Traces on IN625 Bare Plates. Integr Mater Manuf Innov 2020;9:16–30. https://doi.org/10.1007/s40192-020-00169-1.

[46] Thampy V, Fong AY, Calta NP, Wang J, Martin AA, Depond PJ, et al. Subsurface Cooling Rates and Microstructural Response during Laser Based Metal Additive Manufacturing. Sci Rep 2020;10:1–9. https://doi.org/10.1038/s41598-020-58598-z.

[47] Shao J, Yu G, He X, Li S, Chen R, Zhao Y. Grain size evolution under different cooling rate in laser additive manufacturing of superalloy. Opt Laser Technol 2019;119:105662. https://doi.org/10.1016/j.optlastec.2019.105662.